



DEVELOPMENTAL BIOLOGY

Precise alternating cellular pattern in the inner ear by coordinated hopping intercalations and delaminations

Roie Cohen^{1,2†}, Shahar Taiber^{1,3†}, Olga Loza^{1†}, Shahar Kasirer^{1,2}, Shiran Woland¹, David Sprinzak^{1*}

The mammalian hearing organ, the organ of Corti, is one of the most organized tissues in mammals. It contains a precisely positioned array of alternating sensory hair cells (HCs) and nonsensory supporting cells. How such precise alternating patterns emerge during embryonic development is not well understood. Here, we combine live imaging of mouse inner ear explants with hybrid mechano-regulatory models to identify the processes that underlie the formation of a single row of inner hair cells (IHCs). First, we identify a previously unobserved morphological transition, termed “hopping intercalation,” that allows cells differentiating toward IHC fate to “hop” under the apical plane into their final position. Second, we show that out-of-row cells with low levels of the HC marker *Atoh1* delaminate. Last, we show that differential adhesion between cell types contributes to straightening of the IHC row. Our results support a mechanism for precise patterning based on coordination between signaling and mechanical forces that is likely relevant for many developmental processes.

INTRODUCTION

The formation of complex, yet precise, cellular patterns during embryonic development relies on two key aspects: the ability of cells to coordinate their differentiation with their neighbors through biochemical signals and the control of cellular and tissue morphology through cell mechanics. It is often unclear, however, how these two aspects of development are coordinated to produce precise cellular patterns. The concept that morphogenesis relies on coordination between biochemical signals and mechanics has been previously discussed in various contexts (1–3) but has gained substantial strength in recent years due to new advances in imaging and force measurement technologies (4, 5). However, relatively little is known on how such coordination controls a large class of developmental patterning processes involving regular alternating cellular patterns, where neighboring cells acquire distinct regulatory and mechanical properties. In most research to date, formation of such alternating patterns was studied in the context of models such as Turing-type models and signaling-mediated lateral inhibition models (6, 7). Mounting evidence strongly suggests that in many of these examples, mechanical forces also play a crucial role in coordinating developmental patterning (8, 9).

A prime example of an alternating cellular pattern, controlled by both signaling-mediated differentiation and mechanically driven reorganization, is the mammalian hearing organ, the organ of Corti (OoC), located within the cochlea (Fig. 1A). The OoC, one of the most organized tissues in the mammalian body plan, consists of exactly four rows of sensory hair cells (HCs), interspersed by nonsensory supporting cells (SCs), to create an alternating checkerboard-like pattern (Fig. 1A). These four rows are further divided into one row of inner hair cells (IHCs) and three rows of outer

hair cells (OHCs), with a single row of inner pillar cells (IPCs) separating them. This precise organization of sensory HCs is believed to have a crucial role in hearing sensitivity and frequency selectivity in mammals (10, 11).

The OoC initially develops from a disordered undifferentiated prosensory epithelium and gradually differentiates and organizes into an ordered pattern (12). In mice, HC differentiation begins after cells in the OoC exit cell cycle at around embryonic day 14 (E14), reaches a highly organized cellular pattern by postnatal day 0 (P0), and refines into its final form within the first two postnatal weeks. HC differentiation is associated with the expression of the transcription factor *Atoh1*, which is considered to be the master regulator of HC fate and is also one of the earliest markers of differentiation into HCs (13). During its development, the OoC exhibits a spatial developmental gradient along the base-to-apex axis of the cochlea, where the base and the apex are the most and least developed regions, respectively.

The alternating pattern of HCs and SCs in the OoC emerges through a process of Notch-mediated lateral inhibition (13–16). In lateral inhibition, cells compete to differentiate into a primary cell fate (e.g., HCs in the OoC) by inhibiting their neighbors from also adopting the same fate (17). Thus, within a small group of cells, one cell adopts a primary fate, while all its neighbors adopt the secondary fate (e.g., SCs in the OoC), leading to an alternating salt-and-pepper pattern. The inhibition is typically mediated by the Notch signaling pathway, which is a conserved juxtacrine signaling pathway driving communication between neighboring cells (18–21). While lateral inhibition models can generate different types of alternating patterns in either one-dimensional (1D) or 2D cell layers, they cannot produce by themselves highly organized patterns when applied to disordered cell lattices (22, 23). Thus, the highly organized pattern of HCs and SCs in the OoC cannot be solely explained by simple lateral inhibition models.

In a recent study, we used live imaging of inner ear explants and mathematical modeling to show that the precise patterning of the OHC region in the OoC emerges from an initially disordered salt-and-pepper pattern by reorganization processes driven by

¹School of Neurobiology, Biochemistry and Biophysics, George S. Wise Faculty of Life Sciences, Tel Aviv University, Tel Aviv 6997801, Israel. ²Raymond and Beverly Sackler School of Physics and Astronomy, Faculty of Exact Sciences, Tel Aviv University, Tel Aviv 6997801, Israel. ³Department of Human Molecular Genetics and Biochemistry, Faculty of Medicine, Tel Aviv University, Tel Aviv 6997801, Israel.

[†]These authors contributed equally to this work.

*Corresponding author. Email: davidsp@tauex.tau.ac.il

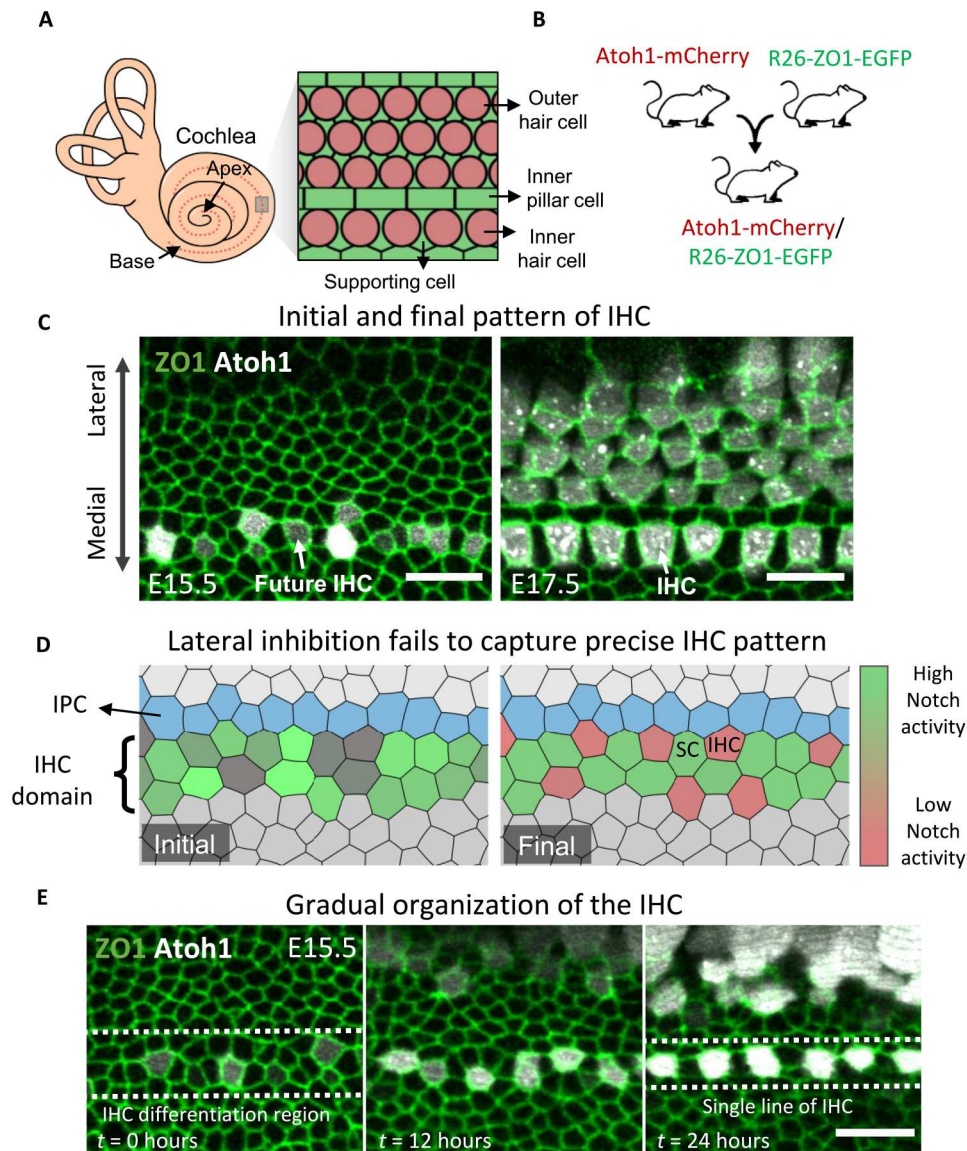


Fig. 1. A single row of IHCs is formed from an initially disordered salt-and-pepper pattern. (A) Schematic of the mammalian inner ear. The dashed line represents the location of the OoC along the cochlea. A zoom-in on the OoC with marked OHCs, IHCs, SCs, and IPCs is presented on the right. (B) Schematic of the transgenic mice used for imaging. Atoh1-mCherry (HC marker) mice are crossed with ZO1-EGFP (tight junction marker) mice to produce double-reporter mice. (C) Snapshots from movies of cochlear explants of a ZO1-EGFP (green)/Atoh1-mCherry (gray) mouse showing initial (left, E15.5) and advanced (right, E17.5) patterns of the IHC row. Double arrow displays the medial-lateral axis. (D) Snapshots from the initial (left) and final (right) time points of a lateral inhibition simulation over a narrow strip of cells (movie S2). Color bar represents the Notch activity level. Initial pattern is resolved to a salt-and-pepper pattern of low Notch activity HCs (red) and high Notch activity SCs (green). The IPCs (blue), the cells below the IHC domain (dark gray), and the cells above the IPCs (light gray) do not participate in the lateral inhibition process. Snapshots shown are sections from a 25-cell-wide simulation window. (E) A filmstrip from a movie of an E15.5 cochlear explant showing the gradual differentiation and patterning of the IHC row (movie S3). Scale bars, 10 μ m.

mechanical forces (22). We have shown that external shear and compression forces acting on the OHC region and repulsion forces between HCs can drive the transition from a disordered to ordered pattern. The pattern is further refined by differential adhesion between OHCs and SCs. Thus, the precise pattern of OHCs is not simply a result of signaling-mediated differentiation (e.g., lateral inhibition) but rather relies on mechanical forces that rearrange the cells into their precise final pattern.

In this work, we explore how the coordination between Notch-mediated lateral inhibition and mechanical forces gives rise to the formation of a single row of IHCs, exhibiting a precise alternating pattern of IHCs and SCs. We used live imaging of inner ear explants from transgenic mice expressing both ZO1-EGFP (Zonula occludens-1 fused to enhanced green fluorescent protein) and Atoh1-mCherry, allowing us to track the morphological dynamics of the cells and their differentiation state, respectively. We found that an initially disordered salt-and-pepper pattern spanning two to three

cell rows is refined by coordinated intercalations and delaminations. In particular, we identified a new type of intercalation termed “hopping intercalation,” allowing cells differentiating toward IHC fate (Atoh1⁺ cells) to “hop” under the apical plane toward the IPC row. We also found that some out-of-row cells that express low levels of Atoh1 delaminate. We developed a hybrid modeling approach, combining a lateral inhibition model with a mechanical 2D vertex model, which captured the main features observed experimentally. We show that further morphological features can be explained by differential adhesion between IHCs, SCs, and IPCs. Predictions generated by our model are validated by tracking rearrangements following laser ablation of single cells. Overall, these results support a picture where mechanics and signaling are coordinated to produce the precise alternating pattern of IHCs.

RESULTS

IHCs differentiate and reorganize into a single row between E15.5 and E17.5

The IHC row in the postnatal cochlea exhibits a precise long-range alternating pattern with very few defects, typically in the form of extra out-of-row IHCs (fig. S1A). To examine how such a precise pattern emerges during development, we used an assay based on live imaging of cochlear explants allowing tracking of both the morphology and the differentiation state of the cells. This was performed by timed mating of transgenic mice expressing ZO1-EGFP, which is a tight junction scaffolding protein (24) typically used as a marker of apical boundaries (25), with transgenic mice that express a transcriptional reporter, Atoh1-mCherry, which is one of the earliest markers for differentiation into nascent HCs (Fig. 1B and fig. S1B) (26, 27). Cochleae from these double transgenic mice were dissected at different developmental stages (E15.5 and E17.5) and imaged under an incubated microscope for up to 24 hours.

Time lapse movies of cochlear explants at E15.5 allow tracking of the initial stages of differentiation as observed by the emergence of Atoh1⁺ cells (movie S1). Consistent with previous work (12), this differentiation begins at the base and progresses toward the apex, with IHCs emerging before OHCs. Here, we focused on the differentiation of the IHC row. Initial appearance of Atoh1⁺ cells at the apex region of E15.5 cochleae occurs within two to three cell rows at the medial prosensory domain (Fig. 1C, left). By E17.5, Atoh1⁺ cells are organized as one ordered row throughout most of the cochlea (Fig. 1C, right), similar to the pattern observed in the adult ear.

The differentiation into HC and SC fates is driven by the process of Notch-mediated lateral inhibition (13–15). To test whether lateral inhibition can create an ordered pattern of IHCs from a narrow strip of cells, we applied our previously described contact-based model of lateral inhibition (23, 28). For simplicity, we consider only one type of Notch ligand in the model, although both Dll1 and Jag2 have been shown to participate in this process (29). In these simulations, we also assumed boundary conditions where the cells in the medial side of the differentiating cells (Kolliker’s organ) express low levels of Notch ligands. This is based on the observation that cells in the Kolliker’s organ express Jag1 (30, 31). Running our model on a narrow strip of cells results in a salt-and-pepper pattern of HCs surrounded by SCs, albeit without a particular long-range order (Fig. 1D and movie S2). The salt-and-pepper patterns we obtained in the basic lateral inhibition model suggests that lateral inhibition is

not sufficient to explain the highly organized IHC pattern. As we have previously shown for the OHC region (22), cellular reorganization processes may contribute to the formation of a precise pattern. We therefore focused on the dynamics of IHC differentiation using live imaging of inner ear explants at this developmental stage.

To observe the reorganization processes that occur during the patterning of the IHC row, we obtained movies of inner ear explants at early developmental stages. Live imaging of E15.5 cochleae at the apex region showed that an initially disordered salt-and-pepper pattern of Atoh1⁺ cells over two to three cell rows reorganizes into an aligned single row of Atoh1⁺ cells (next to the future IPC row) within ~1 day (Fig. 1E and movie S3). Analysis of these movies revealed local morphological transitions and reorganization processes that contribute to the formation of a single row. We found that Atoh1⁺ cells that do not touch the future IPC row move laterally toward the IPC row soon after their differentiation (fig. S1C). While we cannot determine what drives this lateral motion, we observed frequent cell divisions in the Kolliker’s organ, medial to the developing IHC domain, in agreement with a previous study showing increased cell divisions in the medial part of the cochlear duct (fig. S1D and movie S4) (32). This might suggest that a pressure gradient is generated in the medial-lateral axis, compressing the Atoh1⁺ cells toward the lateral prosensory domain. Such a pressure gradient is expected to act on all the cells and not only on Atoh1⁺ cells; however, it was previously shown that cells that up-regulate Atoh1 detach from the basement membrane and migrate toward the luminal surface (33). This could explain the high mobility of Atoh1⁺ cells relative to other cells that are still connected to the basement membrane.

Atoh1⁺ cells perform “hopping intercalations” toward the IPC border

We found that the lateral movement of Atoh1⁺ cells is accompanied by two morphological transitions: (i) cellular intercalations, as previously shown to occur during the development of the OoC (fig. S2, A to D, and movie S5) (22, 34), and (ii) a newly identified reorganization process, termed hopping intercalation. Hopping intercalation occurs when a cell opens a new apical footprint at an adjacent tricellular junction and then merges with the original apical surface (Fig. 2, A to D, and movie S6). In this process, the cell effectively “hops over” the cellular junction instead of squeezing in as occurs in standard intercalation. To verify that hopping intercalation has a significant role in the patterning process, we have counted the number of intercalations in our movies and found an average of 0.14 ± 0.06 hopping intercalation events and 0.2 ± 0.13 standard intercalation events (of Atoh1⁺ cells intercalating toward to future PC row) per 100 μm per 24 hours (table S1). We find that the apical surface area of Atoh1⁺ cells after hopping intercalation is significantly larger than the surface area before the hopping intercalation (Fig. 2E) and comparable to the surface area of neighboring Atoh1⁺ cells already within the row (fig. S2E). This indicates that the hopping intercalation event is associated with a reduction of mechanical stress at the apical surface of the intercalating cell.

To better understand the mechanics of hopping intercalation, we examined the 3D morphology of the Atoh1⁺ cells during and before hopping. We found that several hours before intercalation (both hopping and standard), the cell body below the apical surface shifts laterally toward the IPC row and seems to be in contact

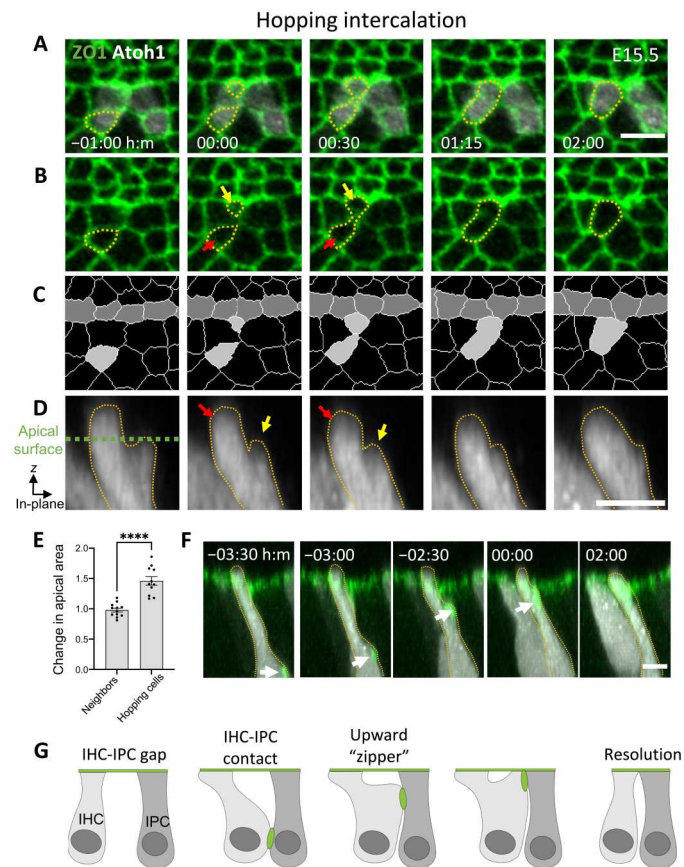


Fig. 2. Hopping intercalation of Atoh1⁺ cells toward the IPC row. (A to C) A filmstrip from an E15.5 cochlear explant showing an apical view of a hopping intercalation event with (A) both Atoh1 and ZO1 markers, (B) only the ZO1 marker, and (C) a segmentation of (B) highlighting intercalating cell (light gray) and IPCs (dark gray) (movie S6). New apical surface opens up [yellow arrow in (B)] and merges with the original apical surface [red arrow in (B)]. (D) A cross section showing a side view of the intercalating cell. The dashed line marks the apical surface of the tissue. Red and yellow arrows mark the original and new apical surfaces of the cell, respectively. (E) Change in apical area of hopping cells. The graph shows the relative change in apical area (area after/area before hopping) for hopping cells. For control, we measured the change in apical area of non-hopping neighboring IHCs at similar times. (F) A cross section of the filmstrip in (A) to (C) [zoomed out with respect to (D)] showing a ZO1 punctum propagating toward the apical surface. Time stamps show time with respect to the initiation of the hopping event (at 00:00 hours:min). (G) A cross section schematic of a hopping intercalation. Statistical test in (E): Welch's *t* test, plot shows means \pm SEM. *n* = 12 and 11 repeats of neighbors and hopping cells, respectively. *****P* < 0.0001. Scale bars, 5 μ m

with it before a new apical surface emerges (Fig. 2F and fig. S2D). To make sure this shift is not an artifact of the ex vivo culture, we additionally examined fixed samples of E15.5 cochleae and observed a similar lateral shift of Atoh1⁺ cells in the apex region (fig. S2F). While the cause for the lateral shift is unknown, this could be a result of the lateral compression discussed previously. In addition, in some cases of hopping intercalations (but also in some standard intercalations), we observed a sub-apical ZO1 punctum at the sub-apical contact point between the Atoh1⁺ cell and the future IPC. This punctum migrates toward the apical surface before the initiation of intercalation and seems to attach the Atoh1⁺ cell to the

future IPC in a zipper-like motion (Fig. 2, F and G, and fig. S2D). As far as we know, this is the first observation of hopping intercalation where a new and noncontiguous apical surface emerges before intercalation. This type of intercalation expands the set of morphological transitions capable of reorganizing epithelial layers.

A hybrid regulatory-mechanical model of hopping intercalations captures IHC patterning

The observation that Atoh1⁺ cells are pushed laterally, resulting in intercalations and hopping intercalations toward the IPC border, may provide a potential explanation for how Atoh1⁺ cells align into a single row. To understand whether these observations are sufficient to explain the IHC row patterning, we developed a hybrid model that incorporates cellular dynamics with a lateral inhibition model (Fig. 3A). To model cellular dynamics, we used a modified 2D vertex model, a well-established approach for simulating dynamics in epithelial tissues (35). In a 2D vertex model, each cell and each cellular boundary can be assigned with different mechanical properties, and the total mechanical energy for the tissue can be defined (fig. S3A). Given an initial state with a predefined set of mechanical parameters, the model modifies the configuration of the vertices such that the total mechanical energy is minimized. In a basic 2D vertex model, each tricellular junction is represented by a vertex, and each cell is represented by a polygon with edges that connect the vertices associated with that cell. To simulate the curvature of the cellular boundaries, we extended the basic 2D vertex model by introducing additional degrees of freedom in the form of virtual vertices on each edge (fig. S3B and Materials and Methods) (36, 37). The modified 2D vertex model can account for nonpolygonal cell shapes (e.g., rounder HCs), as well as morphological transitions involving nonpolygonal cellular deformations.

As hopping intercalation was not previously considered in 2D vertex models, we wanted to find a way to model it such that we capture the qualitative behavior observed experimentally. Hopping intercalation begins with the opening of the second apical surface of the hopping cell and ends at the merger of the two apical surfaces. We model this process as follows: (i) The second apical surface is modeled as an individual cell that is linked to the original cell through the area energy term (fig. S3A). (ii) As the opening of a new apical surface requires an active force to push on the neighboring cells (potentially originated by the cell body "pushing up"), an additional expansion energy term is assigned for the cell representing the new apical surface. (iii) Once the two apical surfaces get close and intercalate, they immediately merge into a single cell. Modeling hopping intercalation in such a way creates a similar hopping process to the one observed experimentally (Fig. 3B and movie S7).

To simulate the effect of hopping intercalations on IHC patterning, we applied a hybrid model combining lateral inhibition and a 2D vertex model that includes hopping intercalation. The two parts of the model are advanced in time in a synchronous manner, allowing for differentiation and morphological dynamics to progress in parallel (see Materials and Methods). On the basis of our observations, the assumptions that we make in the 2D vertex model are the following: (i) Atoh1⁺ cells have higher contractility and incompressibility. This assumption is based on the observed higher circularity of HCs relative to SCs (Fig. 3C) and consistent with our previous observation that HCs are less deformable than SCs (22). (ii) We assume local repulsion force between HCs. This is based on our

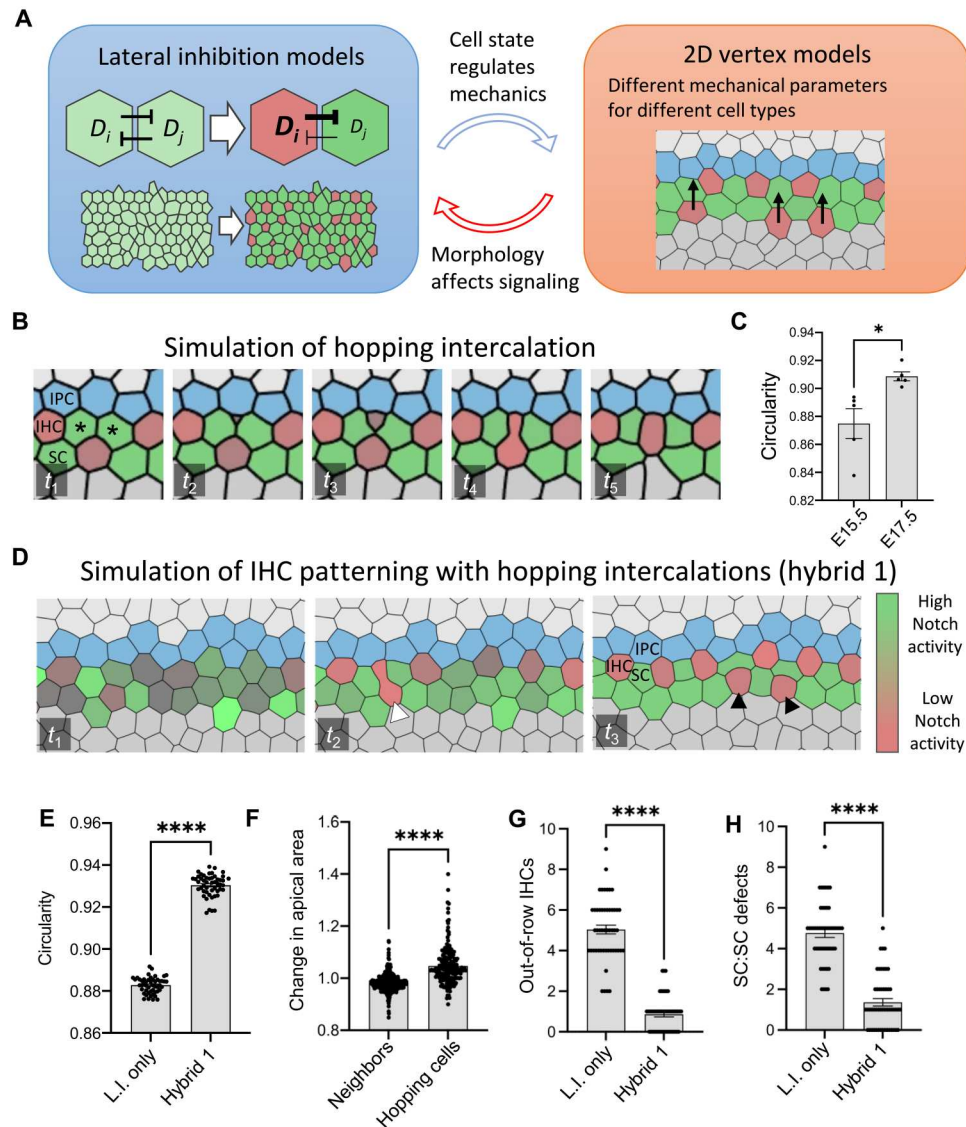


Fig. 3. A hybrid modeling approach incorporating hopping intercalations accounts for reduction in patterning defects. (A) Schematic of the hybrid modeling approach incorporating a feedback between a lateral inhibition circuit (left) and a mechanical 2D vertex model (right; see Materials and Methods for details). (B) A filmstrip of a simulation showing hopping intercalation of an HC. Asterisks mark an SC:SC defect being resolved by hopping intercalation (see Materials and Methods) (movie S7). (C) Comparison between circularity of IHCs at E15.5 and E17.5. (D) A filmstrip of a simulation combining lateral inhibition and hopping intercalations (see hybrid1 model in table S2) (movie S8). The white arrowhead shows an intercalating cell. Black arrowheads show out-of-row IHC defects. Snapshots shown are sections from a 25-cell-wide simulation window. (E to H) Quantitative comparison between a model with lateral inhibition only (L.I. only) and a hybrid model of lateral inhibition and hopping intercalations (hybrid 1 model; see Materials and Methods). Circularity of IHCs (E), number of out-of-row IHC defects (G), and number of SC:SC defects (H) are shown for the two models (average of $n = 50$ simulations). (F) shows relative change in apical area (area after/area before hopping) for hopping cells in the hybrid 1 model. For control, we measured the change in apical area of non-hopping IHCs in the simulation. Statistics: (C, E, and F) Welch's t test; (G and H) Mann-Whitney test; all plots show means \pm SEM. Repeats: (C) $n = 5$ independent movies for each time point, (E) $n = 50$, (F) $n = 175$ and 457 for hopping cells and neighbors, respectively, and (G and H) $n = 50$ simulations. **** $P < 0.0001$ and * $P < 0.05$.

previous observations that HCs physically touch each other at the sub-apical plane corresponding to the position of the nuclei (22). (iii) Atoh1⁺ cells are subjected to a lateral compression force toward the IPCs. This force is applied on all cells whose Atoh1 level crosses a certain threshold. This assumption is based on the observed lateral motion of HCs toward the IPC row (fig. S1C). (iv) Hopping intercalation is initiated for Atoh1⁺ cells whose area decreases below a certain threshold due to the lateral compression.

The new apical surface is created on the boundary of the IPC row (see Materials and Methods). Applying these assumptions to our model (termed hybrid 1 model) captures the lateral movement of Atoh1⁺ cells and hopping intercalations as observed experimentally (Fig. 3D and movie S8). In terms of HC morphology, the hybrid 1 model captures the increase in circularity of IHCs (Fig. 3E, compared to Fig. 3C), as well as the increase in area following the hopping intercalation events (Fig. 3F, compared to Fig. 2E).

To understand whether the hybrid 1 model generates a more ordered pattern of IHCs, we examined the defects in the resulting pattern. We identified two types of defects that occur during the patterning process: the formation of extra HCs that do not border the IPC row (termed out-of-row IHC defects; black arrowheads in Fig. 3D) and the presence of two neighboring SCs with no IHC between them (termed SC:SC defects; asterisks in Fig. 3B). We have compared the number of defects between a model of lateral inhibition without hopping intercalation (L.I.-only model) and the hybrid 1 model that contains hopping intercalation. We find a significant reduction in both types of defects in the hybrid 1 model (Fig. 3, G and H). Thus, we conclude that hopping intercalations help reduce the number of defects and drive the pattern of IHCs to a more organized state. We note, however, that even with hopping intercalations, there are still defects of both types that are not resolved in our model, suggesting the presence of additional mechanisms for defect resolution.

Cells with low Atoh1 levels delaminate

In addition to the intercalations and hopping intercalations, we also noticed that some of the Atoh1⁺ cells that are not aligned against the future IPC delaminate (Fig. 4A and movie S9). Neighboring cells engulf and close the apical footprint of the delaminating cell. During this process, the cell body recedes toward the basement membrane, and the most apical portion of the cell is extruded into the lumen (movie S10 and fig. S4). The observed delaminations contribute to reducing the number of out-of-row IHCs. On average, we observed 0.42 ± 0.29 delaminations per 100 μm per 24 hours in our movies (table S1), which is of the same order as the total number of intercalations (0.34 ± 0.17 per 100 μm per 24 hours). To determine what causes these delaminations, we tested whether there is a correlation between the decision of a cell to delaminate, its Atoh1 level, and its position relative to the IPC row. We find that delaminating Atoh1⁺ cells have, on average, a significantly lower expression level of Atoh1 relative to their nondelaminating Atoh1⁺ neighbors (Fig. 4B). We note that a correlation between Atoh1 levels and cell fate has been demonstrated before, and our observation of delaminations could explain these previous observations (33). Furthermore, most delaminating Atoh1⁺ cells are positioned more medially to nondelaminating Atoh1⁺ cells and do not touch the future IPC row (Fig. 3C). Correspondingly, we find that cells that do not touch the IPC row typically have lower Atoh1 expression (Fig. 3D). We do occasionally observe weak Atoh1⁺ cells that do not touch the IPC row and do not delaminate. It is reasonable to assume, however, that these defects are either resolved through delaminations at a later time point, not captured in our movies, or do not resolve and persist as the sporadic defects observed in the final pattern (fig. S1A). These observations provide a potential mechanism for resolving out-of-row IHC defects and relates the decision to delaminate with a reduced level of Atoh1. Unfortunately, we were not able to track and resolve the final fate of the delaminating cells in our current setup.

It has been previously shown that inhibition of Notch signaling leads to the formation of extra HCs (38, 39). While complete Notch inhibition leads to massive production of HCs and complete disarray of the HC pattern, partial Notch inhibition leads to more subtle phenotypes, exhibiting milder addition of IHCs (30). Moreover, it was previously shown that Dll1 and Atoh1 levels of differentiating HCs are correlated, suggesting a tight connection between Notch

activity and Atoh1 levels (33). We therefore wanted to test how the dynamics of organization are affected by such partial Notch inhibition. We performed live imaging of explants in the presence of subsaturating levels of N-[N-(3,5-difluorophenacetyl)-1-alanyl]-S-phenylglycine t-butyl-ester (DAPT), a γ -secretase inhibitor (fig. S5A and movie S11), and tracked the observed dynamics. We found that partial Notch inhibition leads to the generation of additional Atoh1⁺ cells within 12 to 24 hours after adding DAPT (fig. S5, B and C). We found, however, that some weak Atoh1⁺ cells still delaminate even under such inhibition (fig. S5D). Hence, partial inhibition of Notch signaling leads to the generation of extra Atoh1⁺ cells but is not sufficient to prevent delaminations.

On the basis of these observations, we added a simplified delamination rule to the hybrid 1 model such that each HC that does not manage to border the IPC row within a certain time frame is forced to delaminate (termed hybrid 2 model). As expected, adding this delamination rule to the model completely removes the out-of-row HC defects and produces a more organized alternating pattern of IHCs (Fig. 4E and movie S12). While more complex assumptions associating Atoh1 level and Notch activity with delaminations may provide a more realistic model, we do not currently have sufficient information (e.g., spatial dependence of Notch activity) to incorporate such associations in our model. We note that, as expected, adding delaminations to the model does not further resolve SC:SC defects.

Differential adhesion refines IHC pattern

The model that includes both intercalations and delaminations (hybrid 2 model) can explain the precise alternating order of IHCs and SCs. However, it fails to capture additional morphological features including the increase in alignment of IPCs and the longer contact length between IHCs and IPCs (IHC:IPC contact) compared to the contact length between SCs and IPCs (SC:IPC contact) (Fig. 5, A to C). We reasoned that these morphological aspects may be due to differences in adhesion between the different cell types that dynamically emerge during development. To introduce these changes in the model, we added additional assumptions on the line tensions associated with the IHC:IPC, IHC:SC, and IHC:IHC boundaries (termed hybrid 3 model) (fig. S3A). For simplicity, these changes were introduced as a second stage in the simulation, immediately after reaching the final pattern in the hybrid 2 model. We note that differential adhesion could occur in parallel to IHC differentiation; however, we do observe IPC alignment progressing mostly at later stages (Fig. 5, A to C). The adhesion rules we introduced are as follows: (i) Tensions between IPCs and other cell types (e.g., IHCs and SCs) are higher than tensions between IPCs and other IPCs. Such high tension on the boundary between domains has been shown to promote more straight boundaries in other systems (40). (ii) We assumed that the tension on the IHC:IPC boundary is lower than the tension on the SC:IPC boundary. This assumption is based on the observation that the IHC:IPC contact length is longer than that of the SC:IPC contact length (Fig. 5C). (iii) We assumed very high tension between IHCs. This is based on the observation that in the infrequent occasion that two Atoh1⁺ cells are in contact, the lengths of the contacts are typically very small (see arrowheads in fig. S5A). Simulations of the hybrid 3 model that includes adhesion rules captured the increase in alignment of IPCs (Fig. 5, D and E) and the longer IHC:IPC contact length compared to the SC:IPC boundary (Fig. 5, D and F, and

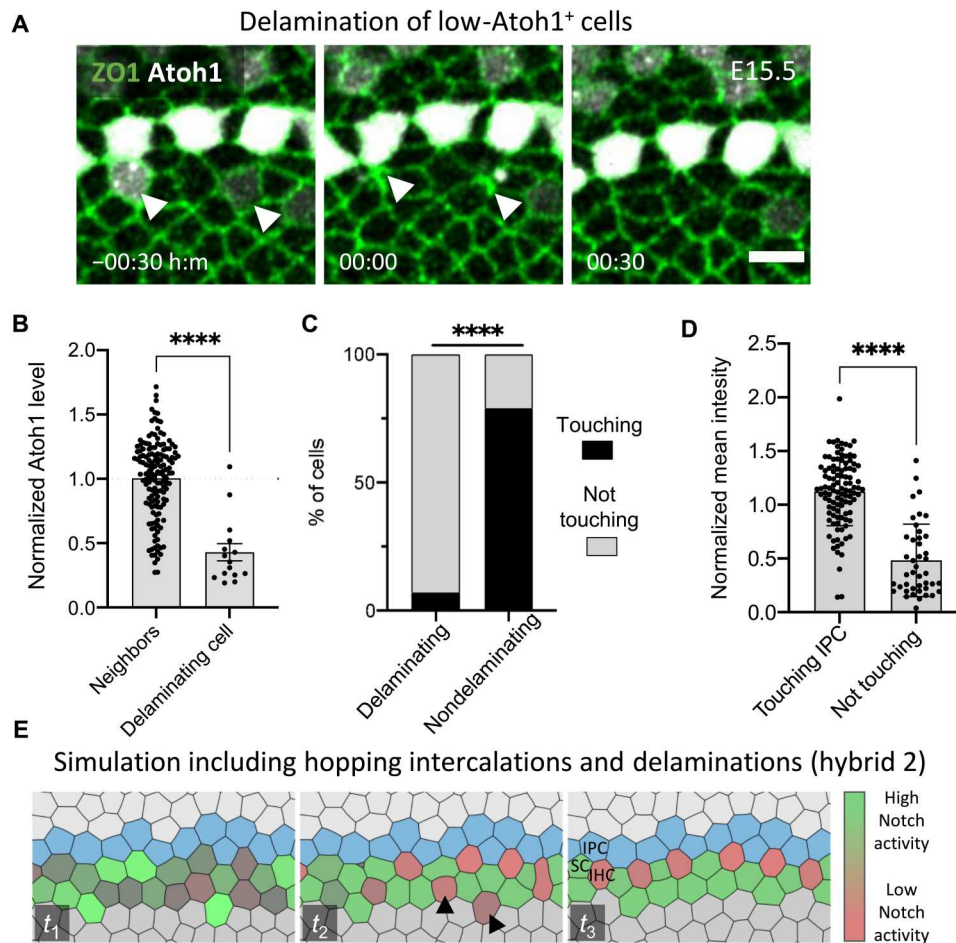


Fig. 4. The IHC pattern is refined by delaminations of low Atoh1⁺ cells. (A) A filmstrip showing delaminations (arrowheads) of low-Atoh1⁺ cells (movie S9). (B) Comparison of normalized Atoh1 levels in delaminating Atoh1⁺ cells versus nondelaminating Atoh1⁺ cells. (C) Comparison of the percentage of IHCs that touch/do not touch the IPC row for delaminating and nondelaminating Atoh1⁺ cells. (D) Normalized Atoh1 level in HCs that touch the IPC row relative to HCs that do not touch the IPC row. (E) Simulation of the patterning process of IHCs that incorporates both hopping intercalation and delaminations of IHCs that do not touch the IPC row (hybrid 2 model) (movie S12). Arrowheads mark two out-of-row IHC defects that were resolved by the end of the simulation. Snapshots shown are sections from a 25-cell-wide simulation window. Statistics: (B and D) Mann-Whitney test; plots show means \pm SEM. (C) χ^2 test. Repeats: (B) $n = 15$ delaminating cells and 150 neighbors, (C) $n = 15$, and (D) $n = 43$ and 106 for cells not touching the IPC row and cells touching, respectively. **** $P < 0.0001$. Scale bar, 5 μ m.

movie S13). We note that longer IHC:IPC contacts are already observed at early stages (E15.5), suggesting that the changes in the tension of IHC:IPC occur before changes in tensions on other boundaries. Overall, the results from the hybrid 3 model show that the addition of adhesion rules between different cell types helps refine the pattern of the IHC row.

Laser ablation experiments support the differential adhesion model

To test the validity of the adhesion rules in the hybrid 3 model, we wanted to generate predictions that can be tested experimentally by applying mechanical perturbations. Local mechanical perturbations can be introduced by ablating single cells and tracking the morphological response around the ablated cell (22). We found that simulating ablation of IPCs, with and without adhesion rules, results in different outcomes. As an initial condition, we used the lattices produced by the hybrid 3 model and then either kept or removed the adhesion rules (see Materials and Methods). In simulations that

include adhesion rules, the IPC row is predominantly repaired by the two IPCs neighboring the ablated cell (Fig. 5G and movie S14). This occurs because a delaminating IPC is more strongly attached to its IPC neighbors and hence “pulls” on them as it delaminates. In contrast, in simulations where the adhesion rules were removed, the probability of repair by the neighboring IPCs is significantly reduced, and there is a higher chance of a break forming in the IPC row (neighboring SCs moving in instead) (Fig. 5H, fig. S6A, and movie S15). To test this prediction, we performed ultraviolet (UV) laser ablation of a single IPC in E17.5 cochlear explants at different positions along the base-to-apex axis, corresponding to different developmental stages. We find that ablation of IPCs in the base region (more advanced stage) mostly results in the repair of the IPC row by neighboring IPCs (Fig. 5I and movie S16). In contrast, ablation in the mid region (less advanced stage) results in a significantly smaller rate of repairs (Fig. 5J, fig. S6B, and movie S17). These results support our hypothesis that the adhesion between IPCs is stronger than the adhesion to their neighbors.

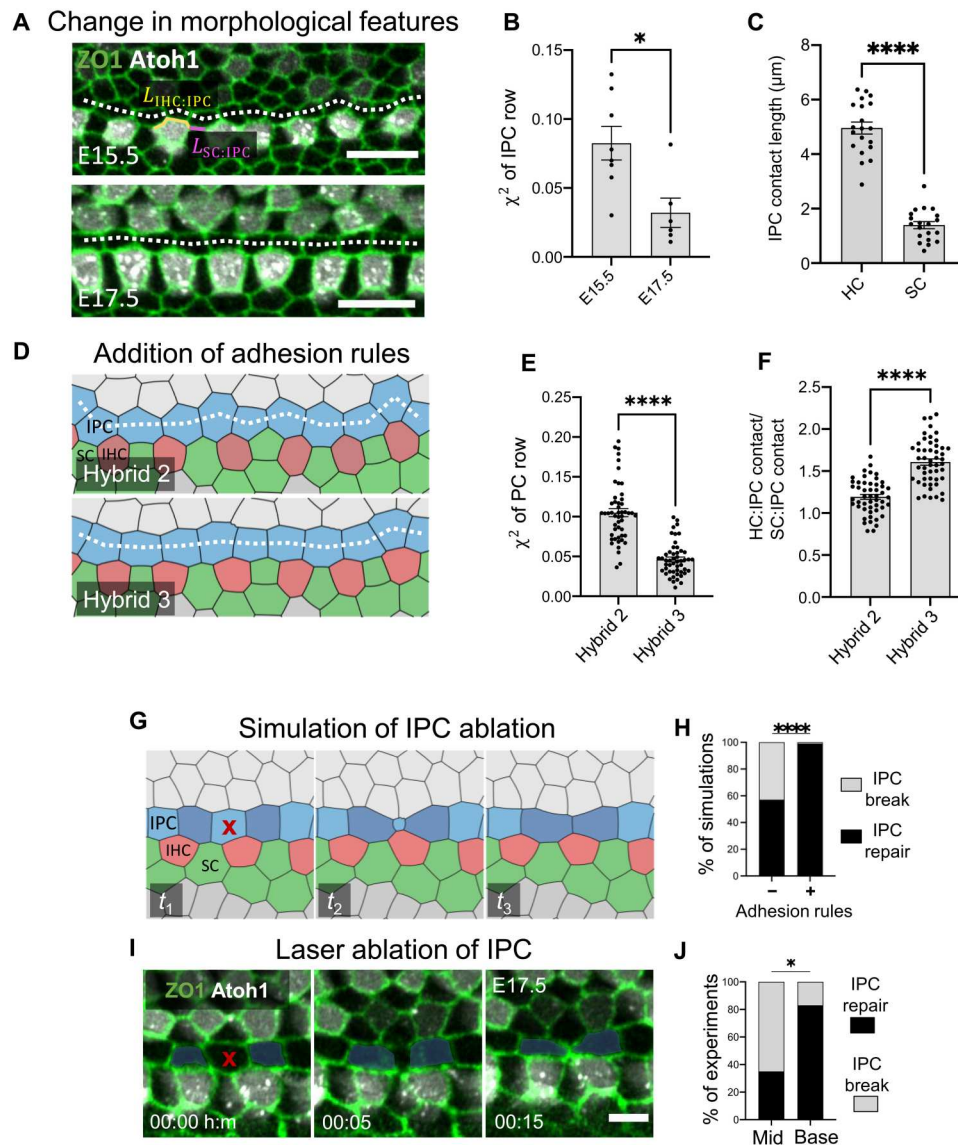


Fig. 5. Differential adhesion underlies straightening of the IHC:IPC boundary. (A) Two images from E15.5 and E17.5 cochlear explants showing the increase in straightness of the IPC row. (B) Quantification of IPC alignment measured by the reduced χ^2 (see Materials and Methods). (C) Comparison of the mean length of IHC:IPC and SC:IPC contact at E15.5. (D) Comparison between hybrid models that include (hybrid 3) or do not include (hybrid 2) adhesion rules (movie S13). In the hybrid 3 model, tension (IPC:SC) = tension (IHC:IHC) > tension (IPC:IHC) > tension (IPC:IPC). Snapshots shown are sections from a 25-cell-wide simulation window. (E) Quantification of IPC alignment for the two models. (F) Ratio between the mean length of IHC:IPC and SC:IPC boundaries in the two models. (G) Filmstrip of a simulation from the hybrid 3 model, where IPC row is repaired (dark blue) after a single IPC was ablated (red "x") (movie S14). (H) Fraction of simulations that resulted in repair of the IPC row in the two models. (I) A filmstrip from a laser ablation experiment performed at the base region of an E17.5 cochlea, where a single IPC was ablated (red "x") (movie S16). (J) Fraction of IPC ablation experiments that resulted in the repair of the IPC row by neighboring IPC. Statistics: (B and F) Student's *t* test, (C) Welch's *t* test, and (E) Mann-Whitney test; plots show means \pm SEM. (H and J) χ^2 test. Repeats: (B) *n* = 7 for E15.5 and *n* = 6 for E17.5; (C) 20 boundaries of each type from *n* = 4 movies, (E and F) *n* = 50, (H) *n* = 150, and (J) *n* = 17 mid and *n* = 12 base. *****P* < 0.0001 and **P* < 0.05. Scale bars, 10 μ m (A) and 5 μ m (I).

Nectins accumulate at the boundaries between IHCs and IPCs

The adhesion rules described above suggest the presence of dedicated molecular mechanisms that promote differential adhesion between different cell types. Earlier work has shown that differential adhesion in the OoC could be mediated by cell adhesion molecules from the Nectin family, known to promote heterophilic interactions. It was shown that Nectin-1 and Nectin-3 are differentially expressed in HCs and IPCs, respectively, and that knockout of Nectin-

1 or Nectin-3 results in patterning defects (41). To determine the distribution of Nectins in the relevant developmental window where IHC patterning is established, we immunostained E15.5 cochleae for Nectin-1 and Nectin-3. We observed the emergence of a polarized accumulation of Nectin-1 and Nectin-3 at the boundary between IHCs and IPCs (Fig. 6 and fig. S7). Nectin accumulation correlates with the emergence of the IHC pattern, showing stronger accumulation at the IHC:IPC boundary at the more developmentally advanced base region. This observation may suggest that the

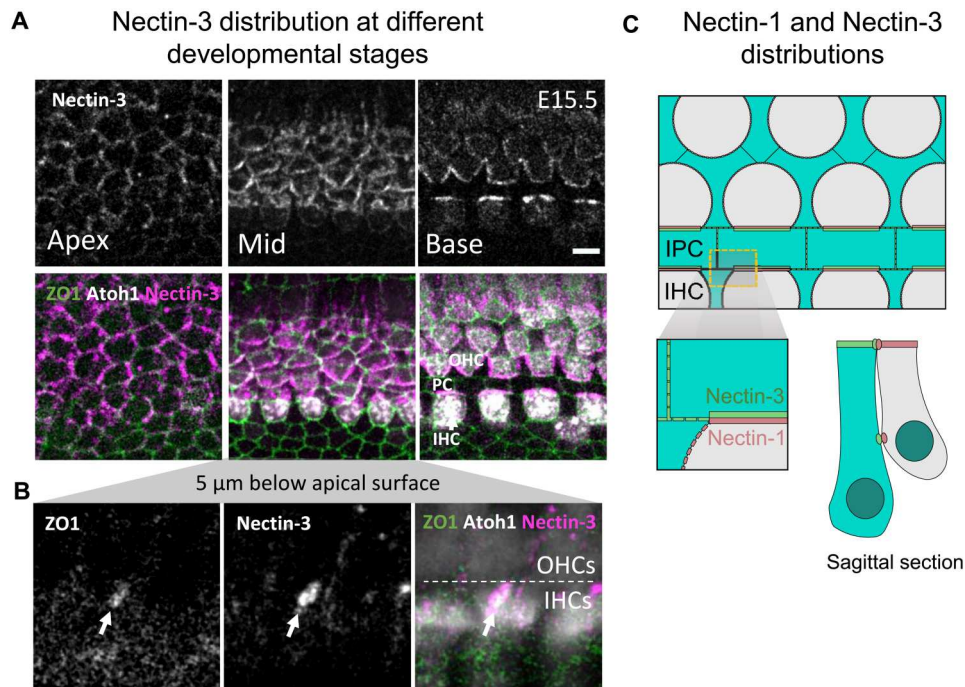


Fig. 6. Nectin-3 accumulation at the IHC:IPC boundary correlates with onset of patterning. (A) Antibody staining of an E15.5 cochlea with α -Nectin-3 antibody. Nectin-3 becomes localized to the IHC:IPC boundary in the more developmentally advanced base region. (B) An image of a sub-apical plane in the mid region, showing a colocalized punctum of ZO1 with Nectin-3. The dashed line marks the IPC boundary, separating between the IHCs and OHCs. (C) Schematic of the localization of Nectin-1 and Nectin-3 in the apical and sub-apical domains. Scale bar, 5 μ m.

preferred adhesion of IHCs to IPCs is mediated by heterophilic Nectin interactions. We also identified several puncta at a subapical level where Nectin-3 is colocalized with ZO1 (Fig. 6B). We did not observe such colocalization with Nectin-1, which we attribute to the poorer sensitivity of our Nectin-1 antibody staining. The colocalization between Nectin-3 and ZO1 in a subapical puncta suggests that the subapical contact between IHCs and IPCs (“the zipper mechanism”) may also be driven by Nectin interactions.

DISCUSSION

In this study, we examined the process by which a single row with a precise alternating pattern of IHCs and SCs emerges during embryonic development. We found that an initially disordered two to three cell row-wide salt-and-pepper pattern is reorganized into a single row by a combination of two main processes: (i) hopping and standard intercalations of Atoh1⁺ cells toward the IPC row and (ii) delaminations of out-of-row Atoh1⁺ cells, typically with low Atoh1 levels. These two processes help resolve the two main types of defects in the initial pattern: SC:SC defects and extra out-of-row Atoh1⁺ cells. Further refinement of the pattern is achieved by differential adhesion between IHCs, SCs, and IPCs. This differential adhesion promotes straightening of the IHC:IPC boundary and longer contact length between IHCs and IPCs.

To elucidate the mechanism driving IHC patterning, we developed a hybrid modeling approach that captures the dynamics of regulatory circuits driven by cell-cell signaling (i.e., Notch signaling), the morphological transitions driven by mechanical forces, and the feedback between the two. More specifically, in our model, the differentiation into HCs and SCs affects the mechanical

properties of the cells and the forces applied on them. In parallel, morphological transitions (e.g., intercalations and delaminations) and cellular morphology (e.g., apical area and boundary curvature) affect signaling by changing the identity of neighboring cells and contact length between them. Despite being based on relatively simple assumptions, the model shows that a combination of intercalations, hopping intercalations, and delaminations is sufficient to resolve most defects formed in the initial salt-and-pepper pattern and generate a highly organized single row of alternating IHCs and SCs. We note that our model does not take into account more complex regulatory relations that may affect cell fate decisions. For example, it has been shown that different Notch ligands (Dll1, Jag1, and Jag2) and Notch regulators (e.g., Lfng and Mfng) are expressed in spatial gradients that affect Notch activity (16, 29, 30). Incorporating such spatial dependence of Notch activity in the model may help explain observations such as the low Atoh1 level in out-of-row cells and the decision of some of these cells to delaminate.

In this work, we modeled the dynamics of our system using 2D vertex models that account for the forces and cellular interactions at the apical surface of the tissue. While it is clear that the complex 3D structure of HCs and SCs plays a role in patterning, we chose to use the simplified 2D vertex models, to reduce the number of parameters and computational complexity. Forces that likely emanate from subapical domains are encoded in our model as external forces acting on the apical surface. While simplified, our model succeeds in capturing the emergence of the precise alternating pattern of the IHCs and in predicting the dynamics following single-cell laser ablation. More detailed understanding of the morphological

transitions observed may require a more complex modeling approach that takes the 3D structure of the cells into account [e.g., 3D vertex models (42–44)].

We have shown that a major process contributing to IHC patterning is the hopping intercalation mechanism. This previously unobserved morphological transition expands on the standard “tool set” of morphological transitions that are typically observed during epithelial morphogenesis (e.g., intercalations and delaminations) and is a result of complex sub-apical cellular dynamics and interactions. A somewhat related mechanism recently observed is that of radial intercalations, where basal cells migrate apically and open a new apical footprint at tricellular junctions (45). In contrast to radial intercalations, cells performing hopping intercalations are cells that already have an existing apical surface, and the general direction of the motion is lateral rather than radial. The basolateral shift of the cell body of the intercalating cell resembles, to a certain degree, the basolateral movement of ectoderm cells in *Drosophila* embryos, in which the cell body rosette formation precedes an apical rosette formation (46). However, in the rosette formation, no new apical surface is formed before the intercalation. Nevertheless, it would be interesting to compare the molecular mechanisms of the basolateral shifts in the mammalian inner ear and the *Drosophila* ectoderm.

While we do not currently know what drives the hopping intercalations in the direction of the IPC, we suggest two mechanisms that are involved in this process: First, the lateral motion of IHCs suggests an external compression acting on IHCs toward the IPC row, possibly driven by cell divisions in the adjacent Kolliker organ (or other morphological processes). We note that we have previously suggested a similar compression (albeit also accompanied by shear) acting on OHC driving their organization (22). Atoh1⁺ cells detach from the basal membrane as they differentiate (33) and become more mobile compared to SCs, which remain attached. Second, the formation of sub-apical ZO1 puncta and its gradual motion toward the apical surface (i.e., the “zipper mechanism”) suggest that once adhesion between these cells is formed, it pulls the two cells together. The observation that these ZO1 puncta sometimes colocalize with Nectins at the contact between differentiating IHCs and IPCs suggest a molecular mechanism for the specificity of the interaction between these two cell types. Both of these mechanisms imply that forces acting at the sub-apical level can affect apical dynamics. Hence, HC patterning is a prime example for a situation where apical morphology is controlled by sub-apical dynamics, a process that is usually overlooked in most studies of epithelial morphogenesis.

The observation that some Atoh1⁺ cells delaminate raises the following questions: What drives the decision to delaminate? What happens to the delaminating cells? We have shown that delaminating cells often have lower Atoh1 levels than their surrounding Atoh1⁺ cells. Recent work tracking Atoh1 activity and nuclear position in cochlear explants showed that Atoh1 level correlates with differentiation into HCs. While most Atoh1⁺ cells move apically as they differentiate, some cells expressing lower levels of Atoh1 initially move apically but then regress and move basally (33). Together with our observations, this supports a picture where Atoh1 levels need to cross a certain threshold to support commitment to HC fate and for Atoh1⁺ cells to maintain their apical footprint. In our current imaging setup, we did not have sufficient temporal resolution to track the fate of delaminating Atoh1⁺ cells and thus could

not determine their fate. However, the observed extrusion of the apical part of the cell (fig. S4) is similar to that of apoptosing HCs (47, 48). Moreover, earlier work showed that genetic inactivation of Atoh1 in E15.5 cochleae leads to enhanced apoptosis in the prosensory epithelium (49). Hence, it is possible that the delaminating Atoh1⁺ cells apoptose. While apoptosis is a rarely observed event during normal OoC development (49), the number of delaminating cells is relatively low (see fig. S5D and table S1) and restricted to a specific developmental stage and hence could have been overlooked.

Our model suggests that differential adhesion between different cell types helps refine the pattern by straightening the IPC boundaries and adjusting the contact length between IHCs and IPCs. It has previously been suggested that Nectin-mediated interactions drive the alternating HC pattern (41). On the basis of our observations and our model, we do not believe that differential adhesion by itself could be sufficient to drive precise IHC patterning as it could not resolve many of the defects observed. Moreover, Nectin-3 knockout mice show some patterning defects but do not lead to a complete disorganization of the IHCs (50). Hence, we suggest that differential adhesion is not a primary driving force in HC patterning but rather a refinement mechanism.

Overall, this work highlights the process in which the regulatory level driving cellular differentiation and the mechanical level driving morphological transitions are coordinated to establish precise cellular patterning. Given that precise cellular patterns occur in many tissues and organs, the insights and tools developed in this work are likely to be relevant in other developmental systems.

MATERIALS AND METHODS

Mice

Atoh1-mCherry mice were a gift from C. Petit, Institute Pasteur, and were maintained on a C57BL/6 background. Rosa26-ZO1-EGFP mice were a gift from Y. Furuta and F. Matsuzaki from RIKEN Laboratory13 (accession no. CDB0260K) and maintained on a C57BL/6 background. All animal procedures were approved by the Animal Care and Use Committee at Tel Aviv University (04-20-003). Genotyping was performed using the KAPA HotStart Mouse Genotyping Kit (Sigma-Aldrich, KK7352) using primers listed in table S3. For timed mating, one or two females, 8 to 15 weeks old, were paired with an appropriate male for overnight mating. Mice were separated the next morning. All animal procedures were approved by the Animal Care and Use Committee at Tel Aviv University (approval number 08-01-2020). All institutional guidelines for animal care were strictly followed.

Immunohistochemistry

Neonatal mice at P0 were sacrificed by decapitation, and inner ears were dissected directly into cold phosphate-buffered saline (PBS) and fixed in 4% paraformaldehyde (Electron Microscopy Sciences, catalog no. 15710) for 2 hours at room temperature. For whole-mount imaging, sensory epithelia were exposed and separated from the inner ear. Next, samples were incubated in 10% normal Donkey serum (Sigma-Aldrich, catalog no. D9663) with 0.2% Triton X-100 (Sigma-Aldrich, catalog no. T-8787) for 2 hours at room temperature. Samples were then incubated overnight at 4°C in the appropriate primary antibody diluted in antibody diluent buffer (GBI Labs, catalog no. E09-300). Following three washes in PBS, samples were incubated with secondary antibodies for 2 hours at room temperature. Stained samples were mounted on #1 cover

glass slides (0.13 to 0.17 mm thickness) with lateral dimensions of 24 mm by 60 mm (Bar-Naor Ltd., catalog no. BN1052441C) using a fluorescent mounting medium (GBI Labs, catalog no. E18-18). Image acquisition was done with a Zeiss LSM 880 with Airyscan microscope (Zeiss). The following is a list of antibodies and dyes used in this study: anti-MyoVIIa (1:250; Proteus Biosciences, catalog no. 25-6790), anti-Nectin-3 (1:250; GeneTex, catalog no. GTX16913), anti-Nectin-1 (1:250; MBL international corporation, catalog no. D146-3), Alexa Fluor 647 donkey anti-rat (1:500; the Jackson Laboratory, catalog no. 712-605-150), goat anti-rabbit Alexa Fluor 488 (1:250; Cell Signaling, catalog no. 4412s), and phalloidin-iFluor 488 reagent (1:1000; Abcam, catalog no. ab176753).

OoC explants

Cochlear dissection for ex vivo culture was performed as previously described (22). Briefly, cochleae were dissected in cold PBS and placed in a Cellvis four-chamber glass-bottom dish (D35C4-20-1.5-N) inside 100 μ l of Matrigel Phenol Red Free solution (In Vitro Technologies, catalog no. FAL356237) diluted 1:15 in Dulbecco's modified Eagle's medium. After Matrigel solidified, medium was added, and samples were transferred to the imaging chamber. DAPT treatments: DAPT was diluted according to the manufacturer's instructions in dimethyl sulfoxide (DMSO). The diluted solution was then added to the culture dish at the beginning of the movie to reach a final DAPT concentration of 1 μ M. Control dishes contained the same amount of DMSO without DAPT.

Microscopy details

Cochleae were imaged using a Zeiss LSM 880 confocal microscope equipped with an Airyscan detector using a 488-nm laser for GFP, a 561-nm laser for mCherry, and a 633-nm laser for Alexa Fluor 647. For fixed samples, we used a Plan-apochromat 63 \times oil-immersion objective with a numerical aperture (NA) of 1.4. For live imaging, we used a C-Apochromat 40 \times water-immersion objective with an NA of 1.2. The microscope was equipped with a 37°C temperature-controlled chamber and a CO₂ regulator providing 5% CO₂. The equipment was controlled using Zeiss software—"Zen black."

Laser ablation system

Laser ablation experiments were performed using a Rapp OptoElectronic UGA-42 Caliburn system equipped with a 355-nm UV short-pulse laser. The ablation system was integrated to the microscope's hardware and software and controlled using the Rapp software SysCon. In ablation experiments, cells were hit with 500 short consecutive pulses over 0.5 s with a laser power of 4%.

Image analysis

Images of the OoC were taken as a sequence of focal planes (z-stack) spanning a depth of 20 to 30 μ m with a pixel size of 0.1 μ m and a separation of 0.7 μ m between z-stacks ([0.1, 0.1, 0.7] μ m/voxel). Movies are a sequence of such images with a frame rate of 1/15 min. Laser ablation movies were taken with a smaller field of view and with a faster frame rate of 1/2 min. Data processing was performed offline using custom-built codes in MATLAB (MATLAB R2020b, the MathWorks Inc.) and using the open-source software ImageJ. The presented images and movies were obtained from a custom-made surface projection algorithm in MATLAB (see the "Surface projection" section). Images of sagittal planes were produced by using ImageJ's Orthogonal Views function.

Segmentation of the cellular boundaries was done using the ZO1 channel in the surface projection. The images were preadjusted for segmentation by using a Gaussian blur filter and h-minima transform. Then, a watershed algorithm was applied to get a binary image of the cellular boundaries. Any defects in the segmentation were manually fixed using a custom-made code.

To obtain data of individual cells, we used the labeled segmentation image and the Atoh1 image. HCs, SCs, and IPCs were detected and marked manually according to Atoh1 expression, cell position, and cellular morphology. For each cell, the following data were trivially extracted: apical surface area, cell circumference, Atoh1 expression, and neighboring cells.

Surface projection

Our data are volumetric 3D stacks of sections of the OoC, which contain the apical surface as well as sub-apical surfaces. Since ZO1 is concentrated in tight junctions, we used maximum intensity projection (MIP) to get a 2D projection of the cellular boundaries at the apical surface. For Atoh1, however, MIP creates a projection of the entire cellular volume of HCs, not only from the apical surface. Therefore, using MIP for a two-channel ZO1-Atoh1 image makes it hard to relate Atoh1 expression with a specific cell observed at the apical surface. For that reason, we developed a surface projection algorithm that presents a 2D projection of the apical surface for both ZO1 and Atoh1 as well as reduces off-apical noise.

The first step in the algorithm was to create a stack that roughly represents the apical surface. As ZO1 is brightest at the apical cellular boundaries, we use strong Gaussian blurring (Gaussian sigma, ~ 3 μ m) to get a smooth stack that roughly represents the apical surface (surface stack). The second step is to refine the surface stack and get a 3D mask that represents the apical surface more accurately (surface mask). For that, we started with an empty stack with identical dimensions to the surface stack. Then, for each xy position in the surface stack, we find the z position with the highest ZO1 signal and mark the corresponding voxel in the surface mask as 1. At this point, the surface mask contains 1 at the voxels that represent the apical surface or 0 otherwise. To make the surface mask smoother, we apply a weak Gaussian blur filter (Gaussian sigma, ~ 0.2 μ m). We then multiply the original ZO1 stack and the Atoh1 stack with the surface mask (voxel-to-voxel multiplication). These new stacks contain the signal from the apical surface alone. Last, we take the MIP of these new stacks to get a 2D projection of the apical surface.

Change in apical area after hopping intercalation

To measure the change in apical area of cells that perform hopping intercalations, we measured the apical area of each hopping cell before and after hopping. The first measurement was done one frame before a new apical surface was first observed (~ 15 min before), and the second measurement was done 1 hour after the two apical surfaces were merged, to allow enough time for relaxation. As a control, we measured the apical area of non-hopping IHC neighbors at the same time points. This average change for hopping and non-hopping cells is presented in Fig. 2E.

Circularity of IHC

To assess the roundness of IHCs at different developmental stages, we used the circularity measure. Circularity is defined as $4\pi A/L^2$, where A is the cell apical area and L is the cell circumference. The value range for circularity is 0 to 1, where values closer to 1 indicate

that the shape is closer to a perfect circle. We analyzed images from E15.5 and E17.5 cochleae, indicating early and advanced time points, respectively. For each image, we measured the circularity of 10 randomly chosen IHCs and calculated the average value for that image. We then averaged the circularity values of different images from E15.5 and E17.5 cochlea separately, as presented in Fig. 3C.

Number and Atoh1 levels of delaminating Atoh1⁺ cells

To measure the Atoh1 expression of the cells, we used the mCherry channel in the surface projection and the segmented image. For each cell, we defined the Atoh1 level as the total mCherry intensity of the cell divided by the area of the cell. The intensity of mCherry can vary between different experiments due to differences between mice. Therefore, we defined a normalized Atoh1 level as the Atoh1 level of the cell divided by the average Atoh1 level of the 10 closest neighboring Atoh1⁺ cells. This normalized level indicates the relative intensity of the cell with respect to other Atoh1⁺ cells. For each delaminating Atoh1⁺ cell, the intensity measurement of the cell and its Atoh1⁺ neighbors was performed one frame before the delamination. The averaged normalized intensity of delaminating cells and their neighbors is presented in Fig. 4B.

To link between the decision of Atoh1⁺ cells to delaminate and their position, we counted the number of delaminating Atoh1⁺ cells that touch/do not touch the IPC row at the time of delamination. In addition, we counted the number of nondelaminating Atoh1⁺ cells that touch/do not touch the IPC row at the end of each movie. IPCs were identified by their rectangular morphology. If the analysis was done at a stage where cellular morphology was not yet differentiated, the IPCs were identified at a later time point in the movie, where morphological differences are clear, and then traced back to the analyzed time point. The percentage of delaminating/nondelaminating Atoh1⁺ cells that touch/do not touch the IPC row is presented in Fig. 4C.

Last, to link between Atoh1⁺ cells' position and their Atoh1 level, we calculated the normalized Atoh1 level for each cell that touch/do not touch the IPC row at the initial point of each movie. The averaged intensity for touching/non-touching cells is presented in Fig. 4D.

Effect of Notch inhibition on Atoh1⁺ cells

To investigate the effect of Notch inhibition in early developmental stages, we imaged E15.5 cochlear explants for 3 hours, then treated them with 1 μ M DAPT, and continued imaging for 20 hours. We manually counted the number of Atoh1⁺ cells in the IHC region at the last time point before DAPT treatment and 20 hours after treatment, as well as the number of delaminations of Atoh1⁺ cells during the movies. For each movie, we calculated the ratio between the final and initial number of Atoh1⁺ cells and the number of Atoh1⁺ cells per 100 μ m. As a control, we repeated the same measurements for E15.5 cochlear explants treated with DMSO. The averaged data of the DAPT and DMSO movies are presented in fig. S5 (B to D).

Morphological measurements of the IPC boundary

To estimate the morphological parameters of the IPC row at different developmental stages, we used images from E15.5 and E17.5 cochleae. To estimate the straightness of the IPC row, we manually marked the center of each of the IPCs in each image and used a

modified version of the reduced χ^2 statistic given by

$$\chi_{\text{red}}^2 = \frac{1}{N_{\text{DOF}}} \sum_{i=1}^N \frac{|\vec{r}_i - \vec{r}_{\text{fit}}(i)|^2}{w^2}$$

where N is the number of IPCs, \vec{r}_i is the position of cell i , $\vec{r}_{\text{fit}}(i)$ is the closest point to \vec{r}_i on the best fitted line passing through all marked positions, w is the weight, and $N_{\text{DOF}} = N - 2$ is the degrees of freedom. We chose the weight to be the average horizontal length of an IPC given by $w = |\vec{r}_N - \vec{r}_1| / (N - 1)$. The average χ_{red}^2 of the IPC row in different developmental stages is presented in Fig. 5B.

To measure the contact length between IHC/SC and the IPC row, we segmented the IHC:IPC and SC:IPC boundaries in E15.5 cochleae. For each IHC/SC that touches the IPC row, we measured the total length of its interface with the IPC row (the cell can have boundaries with more than one IPC). The average IPC row contact length for IHCs and SCs is presented in Fig. 5C.

IPC ablation experiment analysis

To determine the effect of mechanical perturbations in the IPC row at different developmental stages, we ablated IPCs in the base and mid regions of E17.5 cochleae. In each experiment, a single IPC was ablated using a UV laser pulse directed at the center of the apical surface of the cell (see the "Laser ablation system" section for more details). Immediately after the ablation, a small region around the ablated IPC was imaged for 30 min with a 1-min interval, during which the continuity of the IPC row was either broken or repaired by the two neighboring IPCs. The percentage of experiments that resulted in IPC row repair/break in the mid/base regions is presented in Fig. 5J. We note that some of the ablation experiments were performed in different positions on the same cochlea, separated by at least 10 cells in diameter. Overall, 13 cochleae were used for IPC ablation experiments.

Lateral inhibition model

We simulate lateral inhibition patterning based on our previously described cell-cell contact-dependent lateral inhibition model (23) that incorporates the assumption that signaling strength between two cells is proportional to the contact area between the cells. This is a simplified model that assumes only one kind of receiver, Notch, and one kind of ligand, Delta. Furthermore, for simplicity, we considered a model that does not include cis inhibition between receptors and ligands. Here, we present a short summary of the model.

Assume that cell i and cell j are neighbors and share a boundary with a contact length of l_{ij} . We denote Notch concentration in cell i at the boundary with cell j as n_{ij} . Similarly, d_{ij} is Delta concentration in cell i at the boundary with cell j . The signaling scheme is simplified as follows: Notch on cell i interacts with Delta on cell j with an association rate of κ_i^{-1} and produces a signal in cell i proportional to $n_{ij}d_{jl}l_{ij}$. The total repressive signal of cell i , R_i , is increasing with $\sum_j n_{ij}d_{jl}l_{ij}$ until saturation, with the sum being over all the neighboring cells to cell i . Therefore, the unitless dynamical equations for Notch concentration, Delta concentration, and the repressor

expression can be written as

$$\frac{dn_{ij}}{dt} = \frac{\beta_N}{L_i} - n_{ij} - \kappa_i^{-1} n_{ij} d_{ji} \quad (1)$$

$$\frac{dd_{ij}}{dt} = \frac{\beta_D}{L_i} \frac{1}{1 + R_i^l} - d_{ij} - \kappa_i^{-1} d_{ij} n_{ji} \quad (2)$$

$$\frac{dR_i}{dt} = \beta_R \frac{(\sum_j n_{ij} d_{ji} l_{ij})^m}{1 + (\sum_j n_{ij} d_{ji} l_{ij})^m} - \gamma_R R_i \quad (3)$$

where β_N , β_D , and β_R are the production rates of Notch, Delta, and the repressor, respectively; γ_R is the degradation rate of the repressor; L_i is the perimeter of cell i ; and l and m are the Hill coefficients for the repressor and total signal, respectively. For complete details of the lateral inhibition model, see (23).

We note that while Eqs. 1 and 2 account for the change in Notch and ligand concentrations on each boundary separately, they do not explicitly include diffusion over the membrane or a necessary redistribution given a change in cellular morphology. For that, we allow redistribution of receptors and ligands over the total membrane of the cells in parallel to the signaling, which creates an indirect interaction between concentrations on different boundaries of the same cell (see the next section).

Simulations of lateral inhibition model

To run the lateral inhibition model, we need to have a defined tissue geometry and adjacency information of neighboring cells. The geometry of the tissue is defined on the basis of the vertex model, such that each cell is represented by a polygon in a connected network of cells (see the “2D vertex model” section). This representation allows for the definition of neighboring cells and boundary lengths.

As differentiation of IHCs occurs in a narrow region of cells, we define the signaling domain for lateral inhibition as a region of cells spanning two to three rows. As an initial state, cells in the signaling domain start with randomly distributed basal levels of Notch and Delta and no repressor (randomized using additive white Gaussian noise, with a Notch average level of 2 and a ligand average level of 0.1). We note that the initial variability in the expression levels is chosen such that it is not too high to predetermine the cellular fate but not too low so that the lateral inhibition feedback does not take a long time to differentiate between the cells. Cells in the medial side of the signaling domain are kept with a constant low level of Notch ligand but without Notch receptors, to account for the low levels of Jag1 observed in the Kolliker organ (30). All other cells do not express Notch receptors or ligands. Given this defined initial state, the model is advanced in time in an iterative manner, by changing the expression values using the time derivatives in Eqs. 1 to 3 (Euler’s method).

Last, we want to consider the diffusion of Notch and its ligand over the cell membrane. While for each cell the model changes the concentrations of Notch and its ligand on individual cellular boundaries, we assume that these concentrations diffuse across the circumference of the cell in a faster time scale relative to the simulation time steps. To implement this, we homogeneously redistribute the total expression of Notch and its ligand over the cellular boundaries of the cell, at the end of each time step. Simulation

codes for the lateral inhibition model can be found in the public repository <https://doi.org/10.5281/zenodo.7316269>.

2D vertex model

2D vertex models are widely used for simulating the dynamics of epithelial tissues (35). In 2D vertex models, cells in the tissue are represented by a connected network of polygons, with each side of the polygon representing a cellular boundary between neighboring cells and each vertex representing a tricellular junction. In this simplistic description of epithelial tissues, cells can only have straight cellular boundaries with their neighbors; however, in cases where boundary curvature is significant, this description is not sufficient. Since HCs are significantly rounder than other cell types in the OoC, we solve this problem by introducing additional virtual vertices on each cellular boundary, effectively allowing the boundaries to curve (36, 37).

With the geometry of the tissue defined, mechanical energy can be assigned for each cell, cellular boundary, or any other local or external (conservative) force that might act on the cells. The total mechanical energy of the system is the sum of all these terms (fig. S3A). The dynamics of the tissue is determined according to the gradient descent method, by iteratively repositioning all vertices in the direction that minimizes the total mechanical energy of the system (35). To implement a hybrid model that combines cellular dynamics with lateral inhibition, we run both the vertex model and the lateral inhibition model in parallel, such that both models are advanced in time simultaneously (for further details, see the “Simulations of hybrid models” section). Simulation codes for all hybrid models can be found in the public repository <https://doi.org/10.5281/zenodo.7316269>.

Defining cell types

The forces and interactions between cells can be different for different cell types. Therefore, to appropriately define the energy terms in the model, we assign each cell as either HC, SC, IPC, or a general-type cell. HCs and SCs naturally emerge from the signaling domain in which lateral inhibition is applied. Each cell in the signaling domain whose ligand expression passes a certain threshold (chosen as ~50% of the maximal ligand expression) is set as an HC, while the other cells in the domain are considered as SCs. Each cell that borders the signaling domain on its lateral side is set as an IPC. All other cells outside the signaling domain are defined as general-type cells.

Mechanical energy function

The total mechanical energy of the system can be separated into terms resulting from (i) the internal mechanical properties of the cells, (ii) interaction between cells, and (iii) external forces.

Internal energy terms

The internal terms for the energy function account for the compressibility and contractility of the cells. The compressibility accounts for the energy needed to compress the cell and is given by

$$E_{\text{compressibility}} = \sum_{n=1}^{N_c} \frac{1}{2} \alpha_n (A_n - A_{n,0})^2$$

where α_n is the incompressibility of cell n , A_n is the area of the cell, $A_{n,0}$ is the preferred area of the cell, and N_c is the number of cells in the tissue.

The contractility term accounts for the contracting actomyosin cables at the perimeter of the cell and is given by

$$E_{\text{contractility}} = \sum_{n=1}^{N_c} \frac{1}{2} \Gamma_n L_n^2$$

where Γ_n is the contractility of the cell and L_n is the circumference of the cell.

Interaction terms

The interaction terms in the energy function account for the adhesion and repulsion between cells. The adhesion term is given by

$$E_{\text{adhesion}} = \sum_{n=1}^{N_c} \sum_{\langle ij \rangle_n} \gamma_{n'n}^{ij} l_n^{ij}$$

where γ_n^{ij} and l_n^{ij} are the tension and length of the boundary of the cell that lies between vertices i and j , respectively. The second sum is done over all the boundaries of cell n .

The repulsion between cells acts only between HCs and corresponds to the physical contact between HCs at the HC nuclei level. The simplest way to model such repulsion is using a hard-sphere potential; however, such a term is noncontinuous and does not have a well-defined derivative. To capture a similar behavior with a continuous term, we use the following

$$E_{\text{repulsion}} = \sum_{n=1}^{N_c} \sum_{m=1}^{N_c} \sigma_{nm} \left(\frac{D}{|\vec{r}_n - \vec{r}_m|} \right)^\kappa$$

where σ_{nm} is the repulsion strength between cells n and m , κ is the repulsion exponent, D is the effective diameter of the HC nuclei, and \vec{r}_n and \vec{r}_m are the center of mass (COM) positions of the cells. As the repulsion acts only between HCs, we have

$$\sigma_{nm} = \begin{cases} \sigma_0, n, m \in \{\text{HCs}\} \\ 0, \text{otherwise} \end{cases}$$

By setting the repulsion exponent κ to a high value, we create a term with a very strong repulsion for cells with touching nuclei ($|\vec{r}_n - \vec{r}_m| < D$) and a very weak repulsion for cells with non-touching nuclei ($|\vec{r}_n - \vec{r}_m| > D$). Since there should be no long-range repulsion between cells, we set a cutoff distance, such that this term vanishes for $|\vec{r}_n - \vec{r}_m| > 2D$. Notice that since κ is large, the discontinuity we create is negligible.

External forces

We model the lateral compression on HCs as a linear force that acts on HCs in the direction of the IPC row. The energy associated with the compression force is then

$$E_{\text{compression}} = \sum_{n=1}^{N_c} \zeta_n (y_{\text{PCs}} - y_n)^2$$

where ζ_n is the compression force, y_{PCs} is the average y position of the COM of IPC, and y_n is the y position of the COM of cell n . We additionally assume that this compression force does not act on cells that are already close enough to the IPC. To implement this, we add an additional cutoff rule: Once a cell is one cell diameter apart or less from the IPC, the force vanishes. Last, as lateral compression

acts only on HCs, we have

$$\zeta_n = \begin{cases} \zeta_0, n \in \{\text{HCs}\} \\ 0, \text{otherwise} \end{cases}$$

Unitless parameters

For convenience, we choose to work with unitless parameters. The energy function is normalized by $\alpha_0 \bar{A}^2$, where α_0 is the incompressibility of SCs and \bar{A} is the average area of the cells. This accounts for the following transformation

$$\frac{\alpha_n}{\alpha_0} \rightarrow \alpha_n, \frac{\gamma_{ij}}{\alpha_0 \bar{A}^{3/2}} \rightarrow \gamma_{ij}, \frac{\Gamma_n}{\alpha_0 \bar{A}} \rightarrow \Gamma_n, \frac{\zeta_n}{\alpha_0 \bar{A}} \rightarrow \zeta_n$$

$$\frac{A_n}{\bar{A}} \rightarrow A_n, \frac{l_{ij}}{\bar{A}^{1/2}} \rightarrow l_{ij}, \frac{L_n}{\bar{A}^{1/2}} \rightarrow L_n, \frac{y_n}{\bar{A}^{1/2}} \rightarrow y_n$$

Modeling hopping intercalation

To model hopping intercalation in the vertex model, we define a hopping event as a process where a cell opens a new apical surface that expands and lastly merges back into one apical surface. We define three conditions for the initiation of a hopping event: (i) the hopping cell must be an HC, (ii) the hopping cell and the IPC row must be separated by one cellular boundary, and (iii) the area of the hopping cell must be 90% or less than its preferred area. The first and second conditions restrict hopping events to HCs that hop to the IPC row, as observed in our movies. The third condition sets an internal pressure threshold, effectively defining an energy barrier that the cell must overcome to hop over the boundary.

Once a hopping event is initiated, a new apical surface is opened at a tricellular junction at the IPC row. This new apical surface is modeled as a new cell that is linked to the original hopping cell. The new cell initially adopts all mechanical properties and Notch/ligand expression levels of the original cell. The total expression of Notch/ligand is homogeneously redistributed over the boundaries of the two cells, between each two time points of the simulation. The mechanical linkage between the cells is expressed by the following modification to the compressibility energy term

$$E_{n,\text{area}}^{\text{area}} = \frac{1}{2} \alpha_n (A_n + A_n^{\text{new}} - A_{n,0})^2$$

where A_n and A_n^{new} are the areas of the original and new apical surfaces of cell n . This modification captures the fact that the two cells share the same cellular volume. In addition, as the expansion of the new apical surface requires additional energy (that pushes the neighboring cells), we add an expansion force to the new apical surface in the form of

$$E_{n,\text{new}}^{\text{expand}} = \frac{1}{2} q \alpha_n (A_n^{\text{new}} - A_{n,0})^2$$

where q is a positive expansion factor that determines the strength of the expansion force. This force is possibly originated by the cellular body, pushing the new apical surface up.

Initial and boundary conditions

The initial configuration for the lateral inhibition model and for the hybrid 1 and hybrid 2 models is a disordered lattice of cells. To generate disordered cell lattices, we create 10 by 25 hexagonal lattices

and assign random values for boundary tensions (γ_{ij}) and preferable areas ($A_{0,n}$). We then run the vertex model for each lattice and reassign random values for the parameters every few time steps. Once we have a disordered lattice, we define the signaling domain and assign cell types (as described in the “Defining cell types” section). For simplicity, in all simulations, we use periodic boundary conditions at the left-right and top-bottom edges of the cell lattice (boundary conditions on a torus).

Simulations of hybrid models

In this work, we present three hybrid models that combine our lateral inhibition model with different 2D vertex models. The progression of each hybrid model is done by iteratively changing the Notch/ligand expressions of the cells and the cellular configuration of the lattice, at the same time. In parallel, we allow both intercalations and delaminations to take place for each boundary smaller than a defined threshold length and for each cell smaller than a defined threshold area, respectively. In addition, we allow HCs to perform hopping intercalations into the IPC row (see details in the “Modeling hopping intercalation” section).

In the hybrid 1 model, as presented in Fig. 3D, we assume a lateral compression force that acts on HCs and local repulsion force that acts between HCs (see the “Mechanical energy function” section for details). The lateral compression pushes the HCs toward the IPC row and drives either standard intercalations or hopping intercalations. In addition, as HCs have a round morphology (Fig. 3C) and lower deformability relative to SCs (22), we assign HCs with higher contractility (Γ_n) and higher incompressibility (α_n) compared to other cell types.

As described in the Results section, the hybrid 1 model does not account for the observation of delaminating Atoh1⁺ cells. To include this observation, we modify the hybrid 1 model by adding a delamination rule: Each HC that does not touch the IPC row for a long enough period (defined by a threshold) delaminates. Delamination of a specific cell is forced by setting the preferable area to zero and increasing the contractility to a very high value, causing the cell to rapidly shrink below the threshold area for delamination. Adding this simple delamination rule removes all out-of-row IHC defects in the final pattern, as shown in the simulation in Fig. 4E. We refer to this modified model as a hybrid 2 model.

While the hybrid 2 model captures both hopping intercalations behavior and the reduction in the number of defects, it does not capture the longer length of the IHC:IPC boundaries and the high straightness of the IPC row. To include these morphological aspects, we added a second stage to the model (hybrid 3 model), which starts at the final time point of hybrid 2 model simulations. In this stage, we increase the tensions of the HC:IPC and SC:IPC boundaries such that $\gamma_{\text{IHC:PC}} > \gamma_{\text{SC:PC}} > \gamma_0$, where γ_0 is the tension in SC:SC boundaries. In addition, we increase the tension in the HC:HC boundaries. We note that while we introduce the adhesion rules as a second stage to the model, the two stages likely overlap in vivo. The values for all parameters can be found in table S2.

Simulations of single IPC laser ablation

To investigate the effect of the adhesion rules, IPC ablation simulations started at the end of the hybrid 3 model and then the adhesion rules were either kept or removed (setting $\gamma = \gamma_0$ for all cellular boundaries). In each simulation, a single IPC was “ablated” by

setting the preferable area to zero and increasing the contractility to a very high value, causing the cell to rapidly shrink and delaminate. In each set of simulations (with/without adhesion rules), we counted the number of times the IPC row repaired or broke after the ablation. The data are presented in Fig. 5H.

Model result analysis

The measurements of circularity, change in area after hopping intercalation, reduced χ^2 of the IPC row, contact lengths of IHC:IPC, and SC:IPC interface and IPC row break rate after IPC ablation were performed exactly as in the experiments. The number of defects was counted at the final time point of the simulations of the hybrid 1 model (Fig. 3D). Out-of-row HC defect is defined as any HC that does not have a boundary with an IPC. SC:SC defect is defined as an occurrence of two adjacent SCs that both have a boundary with IPCs.

Statistical analyses

Statistical analyses were performed using Prism 8 software (GraphPad, San Diego, CA). The details of the statistical tests used are found in the figure legends. To test data for normality of distribution, the Anderson-Darling, D’Agostino and Pearson, Shapiro-Wilk, and Kolmogorov-Smirnov tests were used. If a dataset did not pass the normality threshold in at least one of these tests, the Mann-Whitney test was used. If data passed normality tests but did not pass the *F* test for comparing variances, Welch’s *t* test was used. If variances were not significantly different, Student’s *t* test was used. For comparison of discrete categorical data, the χ^2 test was used.

Supplementary Materials

This PDF file includes:

Figs. S1 to S7

Tables S1 to S3

Legends for movies S1 to S17

Other Supplementary Material for this manuscript includes the following:

Movies S1 to S17

[View/request a protocol for this paper from Bio-protocol.](#)

REFERENCES AND NOTES

1. A. F. Marée, P. Hogeweg, How amoeboids self-organize into a fruiting body: Multicellular coordination in Dictyostelium discoideum. *Proc. Natl. Acad. Sci. U.S.A.* **98**, 3879–3883 (2001).
2. A. G. Fletcher, M. Osterfield, R. E. Baker, S. Y. Shvartsman, Vertex models of epithelial morphogenesis. *Biophys. J.* **106**, 2291–2304 (2014).
3. I. Salazar-Ciudad, J. Jernvall, S. A. Newman, Mechanisms of pattern formation in development and evolution. *Development* **130**, 2027–2037 (2003).
4. P.-F. Lenne, E. Munro, I. Heemskerk, A. Warmflash, L. Bocanegra-Moreno, K. Kishi, A. Kicheva, Y. Long, A. Fruleux, A. Boudaoud, T. E. Saunders, P. Caldarelli, A. Michaut, J. Gros, Y. Maroudas-Sacks, K. Keren, E. Hannezo, Z. J. Gartner, B. Stormo, A. Gladfelter, A. Rodrigues, A. Shyer, N. Minc, J.-L. Maître, S. Di Talia, B. Khamaisi, D. Sprinzak, S. Tlili, Roadmap for the multiscale coupling of biochemical and mechanical signals during development. *Phys. Biol.* **18**, (2021).
5. Y. Maroudas-Sacks, K. Keren, Mechanical patterning in animal morphogenesis. *Annu. Rev. Cell Dev. Biol.* **37**, 469–493 (2021).
6. J. R. Collier, N. A. M. Monk, P. K. Maini, J. H. Lewis, Pattern formation by lateral inhibition with feedback: A mathematical model of Delta-Notch intercellular signalling. *J. Theor. Biol.* **183**, 429–446 (1996).
7. A. M. Turing, The chemical basis of morphogenesis. 1953. *Bull. Math. Biol.* **52**, 153–197 (1990).

8. R. Cohen, D. Sprinzak, Mechanical forces shaping the development of the inner ear. *Biophys. J.* **120**, 4142–4148 (2021).
9. T. Mammoto, D. E. Ingber, Mechanical control of tissue and organ development. *Development* **137**, 1407–1420 (2010).
10. X. Huang, C. Xu, L. Bai, Is the cochlea coiled to provide sound localization? *EPL* **98**, 58002 (2012).
11. D. Manoussaki, E. K. Dimitriadis, R. S. Chadwick, Cochlea's graded curvature effect on low frequency waves. *Phys. Rev. Lett.* **96**, 088701 (2006).
12. E. C. Driver, M. W. Kelley, Development of the cochlea. *Development* **147**, dev162263 (2020).
13. R. Brown, A. K. Groves, Hear, hear for notch: Control of cell fates in the inner ear by Notch signaling. *Biomolecules* **10**, 370 (2020).
14. C. Haddon, Y. J. Jiang, L. Smithers, J. Lewis, Delta-Notch signalling and the patterning of sensory cell differentiation in the zebrafish ear: Evidence from the mind bomb mutant. *Development* **125**, 4637–4644 (1998).
15. P. J. Lanford, Y. Lan, R. Jiang, C. Lindsell, G. Weinmaster, T. Gridley, M. W. Kelley, Notch signalling pathway mediates hair cell development in mammalian cochlea. *Nat. Genet.* **21**, 289–292 (1999).
16. A. E. Kiernan, N. Ahituv, H. Fuchs, R. Balling, K. B. Avraham, K. P. Steel, M. Hrabé de Angelis, The Notch ligand Jagged1 is required for inner ear sensory development. *Proc. Natl. Acad. Sci. U.S.A.* **98**, 3873–3878 (2001).
17. U. Binshtok, D. Sprinzak, Modeling the Notch response. *Adv. Exp. Med. Biol.* **1066**, 79–98 (2018).
18. D. Henrique, F. Schweisguth, Mechanisms of Notch signaling: A simple logic deployed in time and space. *Development* **146**, dev172148 (2019).
19. R. A. Kovall, B. Gebelein, D. Sprinzak, R. Kopan, The canonical Notch signaling pathway: Structural and biochemical insights into shape, sugar, and force. *Dev. Cell* **41**, 228–241 (2017).
20. C. Siebel, U. Lendahl, Notch signaling in development, tissue homeostasis, and disease. *Physiol. Rev.* **97**, 1235–1294 (2017).
21. D. Sprinzak, S. C. Blacklow, Biophysics of Notch signaling. *Annu. Rev. Biophys.* **50**, 157–189 (2021).
22. R. Cohen, L. Amir-Zilberstein, M. Hersch, S. Woland, O. Loza, S. Taiber, F. Matsuzaki, S. Bergmann, K. B. Avraham, D. Sprinzak, Mechanical forces drive ordered patterning of hair cells in the mammalian inner ear. *Nat. Commun.* **11**, 5137 (2020).
23. O. Shaya, U. Binshtok, M. Hersch, D. Rivkin, S. Weinreb, L. Amir-Zilberstein, B. Khamaisi, O. Oppenheim, R. A. Desai, R. J. Goodyear, G. P. Richardson, C. S. Chen, D. Sprinzak, Cell-cell contact area affects Notch signaling and Notch-dependent patterning. *Dev. Cell* **40**, 505–511.e6 (2017).
24. M. Furuse, Molecular basis of the core structure of tight junctions. *Cold Spring Harb. Perspect. Biol.* **2**, a002907 (2010).
25. F. K. Riesen, B. Rothen-Rutishauser, H. Wunderli-Allenspach, A ZO1-GFP fusion protein to study the dynamics of tight junctions in living cells. *Histochem. Cell Biol.* **117**, 307–315 (2002).
26. P. Chen, J. E. Johnson, H. Y. Zoghbi, N. Segil, The role of Math1 in inner ear development: Uncoupling the establishment of the sensory primordium from hair cell fate determination. *Development* **129**, 2495–2505 (2002).
27. L. Lepelletier, J. B. de Monvel, J. Buisson, C. Desdouets, C. Petit, Auditory hair cell centrioles undergo confined Brownian motion throughout the developmental migration of the kinocilium. *Biophys. J.* **105**, 48–58 (2013).
28. P. Formosa-Jordan, D. Sprinzak, Modeling Notch signaling: A practical tutorial. *Methods Mol. Biol.* **1187**, 285–310 (2014).
29. A. E. Kiernan, R. Cordes, R. Kopan, A. Gossler, T. Gridley, The Notch ligands DLL1 and JAG2 act synergistically to regulate hair cell development in the mammalian inner ear. *Development* **132**, 4353–4362 (2005).
30. M. L. Basch, R. M. Brown II, H.-I. Jen, F. Semerci, J. Depreux, R. K. Edlund, H. Zhang, C. R. Norton, T. Gridley, S. E. Cole, A. Doetzlhofer, M. Maletic-Savatic, N. Segil, A. K. Groves, Fine-tuning of Notch signaling sets the boundary of the organ of Corti and establishes sensory cell fates. *eLife* **5**, e19921 (2016).
31. J. Orvis, B. Gottfried, J. Kancherla, R. S. Adkins, Y. Song, A. A. Dror, D. Olley, K. Rose, E. Chrysostomou, M. C. Kelly, B. Milon, M. S. Matern, H. Azaiez, B. Herb, C. Colantuoni, R. L. Carter, S. A. Ament, M. W. Kelley, O. White, H. C. Bravo, A. Mahurkar, R. Hertzano, gEAR: Gene Expression Analysis Resource portal for community-driven, multi-omic data exploration. *Nat. Methods* **18**, 843–844 (2021).
32. M. Ishii, T. Tateya, M. Matsuda, T. Hirashima, Retrograde ERK activation waves drive base-to-apex multicellular flow in murine cochlear duct morphogenesis. *eLife* **10**, e61092 (2021).
33. T. Tateya, S. Sakamoto, F. Ishidate, T. Hirashima, I. Imayoshi, R. Kageyama, Three-dimensional live imaging of Atoh1 reveals the dynamics of hair cell induction and organization in the developing cochlea. *Development* **146**, dev177881 (2019).
34. E. C. Driver, A. Northrop, M. W. Kelley, Cell migration, intercalation and growth regulate mammalian cochlear extension. *Development* **144**, 3766–3776 (2017).
35. R. Farhadifar, J.-C. Röper, B. Aigouy, S. Eaton, F. Jülicher, The influence of cell mechanics, cell-cell interactions, and proliferation on epithelial packing. *Curr. Biol.* **17**, 2095–2104 (2007).
36. H. J. Frost, C. V. Thompson, C. L. Howe, J. Whang, A two-dimensional computer simulation of capillarity-driven grain growth: Preliminary results. *Scr. Metallurg.* **22**, 65–70 (1988).
37. T. Tamaki, K. Murakami, H. Homma, K. Ushioda, Two-dimensional grain growth simulation by local curvature multi-vertex model. *Mater. Sci. Forum* **715–716**, 551–556 (2012).
38. K. Mizutari, M. Fujioka, M. Hosoya, N. Bramhall, H. J. Okano, H. Okano, A. S. B. Edge, Notch inhibition induces cochlear hair cell regeneration and recovery of hearing after acoustic trauma. *Neuron* **77**, 58–69 (2013).
39. N. Yamamoto, K. Tanigaki, M. Tsuji, D. Yabe, J. Ito, T. Honjo, Inhibition of Notch/RBP-J signaling induces hair cell formation in neonate mouse cochleas. *J. Mol. Med.* **84**, 37–45 (2006).
40. M. Aliee, J.-C. Röper, K. P. Landsberg, C. Pentzold, T. J. Widmann, F. Jülicher, C. Dahmann, Physical mechanisms shaping the Drosophila dorsoventral compartment boundary. *Curr. Biol.* **22**, 967–976 (2012).
41. H. Togashi, K. Kominami, M. Waseda, H. Komura, J. Miyoshi, M. Takeichi, Y. Takai, Nectins establish a checkerboard-like cellular pattern in the auditory epithelium. *Science* **333**, 1144–1147 (2011).
42. H. Honda, M. Tanemura, T. Nagai, A three-dimensional vertex dynamics cell model of space-filling polyhedra simulating cell behavior in a cell aggregate. *J. Theor. Biol.* **226**, 439–453 (2004).
43. S. Okuda, Y. Inoue, T. Adachi, Three-dimensional vertex model for simulating multicellular morphogenesis. *Biophys. Physicobiol.* **12**, 13–20 (2015).
44. S. Alt, P. Ganguly, G. Salbreux, Vertex models: From cell mechanics to tissue morphogenesis. *Philos. Trans. R. Soc. B Biol. Sci.* **372**, 20150520 (2017).
45. J. Sedzinski, E. Hannezo, F. Tu, M. Biro, J. B. Wallingford, Emergence of an apical epithelial cell surface in vivo. *Dev. Cell* **36**, 24–35 (2016).
46. Z. Sun, C. Amourah, M. Shagirov, Y. Hara, T. E. Saunders, Y. Toyama, Basolateral protrusion and apical contraction cooperatively drive Drosophila germ-band extension. *Nat. Cell Biol.* **19**, 375–383 (2017).
47. Y. Raphael, R. A. Altschuler, Reorganization of cytoskeletal and junctional proteins during cochlear hair cell degeneration. *Cell Motil. Cytoskeleton* **18**, 215–227 (1991).
48. T. Anttonen, I. Belevich, A. Kirjavainen, M. Laos, C. Brakebusch, E. Jokitalo, U. Pirvola, How to bury the dead: Elimination of apoptotic hair cells from the hearing organ of the mouse. *J. Assoc. Res. Otolaryngol.* **15**, 975–992 (2014).
49. T. Cai, M. L. Seymour, H. Zhang, F. A. Pereira, A. K. Groves, Conditional deletion of Atoh1 reveals distinct critical periods for survival and function of hair cells in the organ of corti. *J. Neurosci.* **33**, 10110–10122 (2013).
50. T. Fukuda, K. Kominami, S. Wang, H. Togashi, K. Hirata, A. Mizoguchi, Y. Rikitake, Y. Takai, Aberrant cochlear hair cell attachments caused by Nectin-3 deficiency result in hair bundle abnormalities. *Development* **141**, 399–409 (2014).

Acknowledgments: We thank the members of the Sprinzak laboratory and K. Avraham for advice and comments on this work. Atoh1-mCherry mice were a kind gift from Christine Petit, Institut Pasteur, France. ZO1-EGFP mice were a kind gift from Yasuhide Furuta and Fumio Matsuzaki from RIKEN, Japan. **Funding:** This work has received funding from the European Research Council (ERC) under the European Union's Horizon 2020 research and innovation programme (grant agreement no. 682161) and from the Israeli Science Foundation (ISF grant number 1343/22). **Author contributions:** This scientific study was conceived and planned by R.C., S.T., O.L., and D.S. The inner ear explant dissections were performed by S.T., O.L., and S.W. Microscopy and image analysis were performed by R.C., S.T., and S.K. Modeling was performed by R.C. The manuscript was written by R.C., S.T., O.L., and D.S. **Competing interests:** The authors declare that they have no competing interests. **Data and materials availability:** All data needed to evaluate the conclusions in the paper are present in the paper and/or the Supplementary Materials. Source data used to produce the numerical figures can be found in the public repository <https://doi.org/10.5281/zenodo.7316273>. MATLAB codes for lattice generation and running the simulations were uploaded to the public repository <https://doi.org/10.5281/zenodo.7316269>. Requests for the Atoh1-mCherry mice should be submitted to christine.petit@pasteur.fr. Requests for the ZO1-EGFP mice should be submitted to fumio.matsuzaki@riken.jp. These can be provided pending scientific review and a completed material transfer agreement.

Submitted 28 May 2022

Accepted 19 December 2022

Published 22 February 2023

10.1126/sciadv.add2157